



Nickel-aluminum diffusion: A study of evolution of microstructure and phase

Alimadadi, Hossein; Kjartansdóttir, Cecilía Kristín; Burrows, Andrew; Kasama, Takeshi; Møller, Per

Published in:
Materials Characterization

Link to article, DOI:
[10.1016/j.matchar.2017.05.039](https://doi.org/10.1016/j.matchar.2017.05.039)

Publication date:
2017

Document Version
Peer reviewed version

[Link back to DTU Orbit](#)

Citation (APA):
Alimadadi, H., Kjartansdóttir, C. K., Burrows, A., Kasama, T., & Møller, P. (2017). Nickel-aluminum diffusion: A study of evolution of microstructure and phase. *Materials Characterization*, 130, 105-112.
<https://doi.org/10.1016/j.matchar.2017.05.039>

General rights

Copyright and moral rights for the publications made accessible in the public portal are retained by the authors and/or other copyright owners and it is a condition of accessing publications that users recognise and abide by the legal requirements associated with these rights.

- Users may download and print one copy of any publication from the public portal for the purpose of private study or research.
- You may not further distribute the material or use it for any profit-making activity or commercial gain
- You may freely distribute the URL identifying the publication in the public portal

If you believe that this document breaches copyright please contact us providing details, and we will remove access to the work immediately and investigate your claim.

Abstract:

Microstructural and phase evolution of an aluminum deposit on nickel, after heat treatment at 883 K, is studied by means of various microscopy techniques, i.e. energy dispersive X-ray spectroscopy, backscattered electron imaging, electron backscatter diffraction, ion channeling contrast imaging and scanning transmission electron microscopy. AlNi_3 crystallites are observed on the aluminum grain boundaries after only 3 min. of heat treatment indicating that nickel and nickel rich phases are the initially diffusing and forming species. Heat treatment for 120 min. or longer results in the formation of Al_3Ni_2 and a porous $\text{Al}_3\text{Ni}_2/\gamma\text{-Al}_2\text{O}_3$ structure at the surface. The Al_3Ni_2 layer is composed of two different grain morphologies, indicating the position of a Kirkendall plane, and hence, there is a high diffusion rate of aluminum in this phase.

1. Introduction:

The aluminum-nickel system and diffusion within the system is of very high importance for large scale applications such as high temperature alloys [1-4] and semiconductor technology [5-8]. Hence, understanding the mechanism(s) of microstructure evolution is of general interest and there is a large body of work on the topic [8-13]. AlNi and AlNi₃ are specifically important for high temperature applications. However, for other applications such as catalysis by high activity nickel, phases containing low concentrations of nickel such as Al₃Ni and Al₃Ni₂ are of higher importance [14]. But, there is (relatively) less research on these phases. The high surface area nickel based electrocatalyst is often produced by selectively leaching element(s) from nickel based alloys [15-19]. Electrodeposition, powder pressing and thermal spraying are well-established techniques for synthesis of the leachable nickel based alloys [16, 17, 19-21]. In previous studies, some of the authors presented a method for synthesis of leachable aluminum-nickel alloys by physical vapor deposition (PVD) of aluminum on nickel and subsequent thermal treatment at 883 K of the aluminum-nickel couple [22, 23]. It was shown that the alloy composition and the thickness of the aluminum-nickel alloy play important roles in the nickel activation process and final performance of the electrocatalyst [22, 23]. Accordingly, for the development of more efficient and durable nickel based (electro)catalysts, evolution of microstructure and phase, as well as understanding the formation mechanism(s) of Al₃Ni and Al₃Ni₂, is of high importance.

In the current paper, the results of thorough microscopical studies on the aluminum-nickel diffusion are communicated and the underlying mechanism(s) of microstructure evolution is discussed. Special emphasis is put on the characterization of the less studied Al₃Ni₂.

2. Experimental

2.1 Material

A commercially available rolled and annealed ~500 μm thick nickel plate was used as the substrate for PVD aluminum. The purity of the nickel substrate was 99 at.%, determined using optical emission spectroscopy. The average grain size of nickel was about 20 μm . In order to ensure removal of all organic residues from the surface, the nickel substrate was cathodically electrocleaned in an electrolyte of the following composition: 16.25 $\text{g}\cdot\text{dm}^{-3}$ NaCN, 16.25 $\text{g}\cdot\text{dm}^{-3}$ Na_2CO_3 , and 54.16 $\text{g}\cdot\text{dm}^{-3}$ NaOH. The electrocleaning was applied potentiostatically at 5 V for 5 min using a stainless steel sheet as the counter electrode (anode). After electrocleaning, the nickel substrate was fully rinsed with deionized water, blown dried with cold air, and introduced into the deposition chamber. The nickel oxide was removed from the surface by means of Ar sputtering in the chamber. A layer of aluminum was deposited onto the nickel substrate by non-reactive DC-magnetron sputtering, using a CC800/9 SinOx coating unit from CemeCon AG. An aluminum 1050 alloy was used as the target. The coating was not of uniform thickness over the substrate but the average thickness is 12 μm . The aluminum deposited nickel plate was cut into suitable sizes of $5\times 10\text{ mm}^2$.

The cut pieces were heat-treated in an atmospheric furnace at $883 \pm 5\text{ K}$ for various times: 0, 3, 10, 20, 30, 120, 240, 360, 480, and 1440 min. After heat treatment, the pieces were removed from the furnace and cooled under ambient conditions.

2.2 Sample preparation for microscopy

For general cross sectional investigations, the cut pieces were hot-mounted in PolyFast resin from Struers, ground down to 4000 grit (SiC) and subsequently polished with 3 and 1 μm diamond pastes.

For detailed microscopic characterization where electron backscattered diffraction (EBSD) was applied, the cut pieces were mounted onto a custom made sample holder developed for cross sectional sample preparation. The samples were ground down to 4000 grit and polished with 3, 1

and 0.25 μm diamond pastes followed by mechanical/chemical polishing with 0.04 μm colloidal silica (OPS from Struers). Finally, in order to achieve high surface quality for EBSD measurements, flat surfaces were prepared using a focused ion beam (FIB) in an FEI Helios NanoLabTM 600 dual beam scanning electron microscope (SEM). The surface preparation with FIB included (i) platinum deposition using a gas injection system and (ii) two step removal of 750 nm of the cross-section (for the details see [24]).

For transmission electron microscopy (TEM), an electron transparent lamella specimen was prepared at an acceleration voltage of 30 kV using the FIB in-situ lift-out technique [25] in the Helios NanolabTM 600. For the final step (amorphous layer removal), a 2 kV Ga^+ beam with a current of 30 pA was applied at an incident angle of 7° , for both sides of the lamella for 10 min to remove surface damage layers during FIB preparation.

2.3 Electron / Ion microscopy

General microstructural and elemental investigations were carried out on all samples in a Hitachi TM3000 Tabletop SEM equipped with a Bruker Quantax 70 energy dispersive X-ray spectroscopy (EDS) system. Based on these general investigations, detailed microscopical analyses were carried out on the following samples: (i) as-deposited, (ii) heat treated for 10 min. and (iii) heat treated for 120 min. Ion channeling contrast imaging (ICCI), simultaneous EBSD and EDS were performed in a dual beam FEI Helios NanoLabTM 600, equipped with an EDAX-TSL EBSD system a Hikari camera and an Apollo 10 silicon drift detector. The ICCI investigations were performed using Ga^+ ions with an energy of 30 keV.

The EBSD measurements were performed in a hexagonal grid with an electron probe current of 5.5 nA at an acceleration voltage of 15 kV. The cleaning procedure of the measured EBSD data was applied using OIM 6TM as follows: (i) grain confidence index standardization, (ii) single iteration grain dilation (in both cases, a grain was defined as a region consisting of at least four connected

points with misorientations of less than 5°), (iii) all the data points with a confidence index below 0.1 were disregarded [26].

The sample heat-treated for 120 min. was studied further in an FEI Titan 80-300ST field-emission-gun TEM, equipped with an EDS (Oxford Instruments, X-MaxN 80 mm² silicon drift detector) and a spherical aberration probe corrector. The microscope was operated at 300 kV in the scanning TEM (STEM) mode and the images were acquired using either a bright-field (BF) or a high-angle annular dark-field (HAADF) detector (the inner detector angle was used at 57 mrad). STEM-EDS measurements were carried out with an interval of 10 nm from a region of 100×200 nm².

2.4 electron backscatter pattern simulation

To achieve accurate phase identification, ESPRIT DynamicS from Bruker was used to simulate electron backscatter patterns (EBSPs) of different aluminum-nickel phases based on the dynamical theory of electron diffraction [27]. Simulations were carried out for an acceleration voltage of 15 kV and image resolution of 512 pixels. Afterwards, the simulated pattern was cross-correlated with the experimentally measured pattern to find the best fit between the two.

3. Results

3.1 General imaging and compositional characterization

In order to characterize the microstructure in the as-deposited state, ICCI was applied and the corresponding micrograph is shown in Fig. 1. The microstructure is composed of fine equiaxed grains adjacent to the substrate (approximately 250 nm in size) and larger grains further away from the substrate of about 1 μm in size.

Fig. 2 shows backscattered electron (BSE) micrographs of the cross section of the as-deposited sample and after heat treatment at a constant temperature of 883 K as a function of time. The large difference in the BSE intensity between aluminum and nickel (Z contrast) is beneficial for initial

investigation of the microstructural evolution upon heat treatment. As can be seen in Fig. 2, after heat treatment for 3 min. some bright (hence, relatively high atomic number) particles are formed within the aluminum layer. After heat treatment for 10 min., the number and the size of bright particles increase. Furthermore, two sharply defined layers between the nickel substrate and aluminum deposit form. EDS analysis revealed that the chemical composition of the layer adjacent to the nickel substrate is very close to Al_3Ni_2 and that of the layer adjacent to the aluminum deposit is close to Al_3Ni . Longer heat treatment up to 30 min. gives rise to further development of the Al_3Ni_2 and Al_3Ni layers. Heat treatment for 120 min. brings about the formation of a porous layer at the very top surface and formation of two new layers close to the nickel substrate. Heat treatment for longer times, i.e. 240, 360, 480 and 1440 min. (not shown in Fig. 1 for 360 and 480 min.) results in a slow thickening of all these three layers at the expense of Al_3Ni_2 layer. Chemical composition analyses using EDS revealed that the chemical compositions of the two layers adjacent to the substrate is very close to AlNi and AlNi_3 , as indicated on the Fig. 2. It is noted that the BSE micrographs reveal the presence of equiaxed grains in the Al_3Ni_2 layer only faintly due to the orientation contrast (but not Z contrast). The average grain size of Al_3Ni_2 layer increases with increasing time, i.e. from 30 to 1440 min. It is worth mentioning that the intermetallic layer thickness seems to change inconsistently. Most notably, the diffusion layer after 20 min. of heat treatment is thicker than that after 30 and 120 min. This stems from the fact that the PVD aluminum thickness in the as-deposited state is not the same all over the substrate, and there is a variation. Hence, the thickness of intermetallic layers varies depending on the aluminum layer thickness in as-deposited state.

General BSE imaging and compositional characterization using EDS has shortcomings in identifying (i) particles forming within the aluminum layer for heat treatment time shorter than 30 min. due to the large X-ray generating volume under the electron beam (i.e. a fully reliable

quantitative EDS is not applicable) and (ii) the top porous layer, since some part of porosity is filled with foreign compounds (resin from the cross-sectional sample preparation). Based on the general imaging characterization, the samples heat treated for 10 and 120 min. incorporate all the phases and microstructural features, including particles within the aluminum layer and top porous layer. Hence, these two samples were chosen for further detailed microscopic characterization.

3.2 Detailed microscopical characterization

10 min. heat treatment

Using the forward scatter electron (FSE) detector located at the bottom of the EBSD detector, the cross-section of the aluminum-nickel diffusion couple is shown in Fig. 3a. There are two main observations.

(i) Two distinct layers are revealed in the micrograph between the aluminum layer and nickel substrate. The elemental map of nickel obtained by EDS which is shown in Fig. 3b, reveals that the two layers are distinct in chemical composition, Al_3Ni and Al_3Ni_2 color coded with green and yellow, respectively.

(ii) Aluminum grains are still of 1 μm average width (see also Fig. 3c) and the particles formed within the aluminum layer are mainly located on the triple junctions and grain boundaries (see also Fig. 3d). Note that the elemental map (Fig. 3b) reveals that these particles are richer in nickel compared to the surrounding aluminum which is in good agreement with the result that the particles appeared brighter in the BSE images. Since these features are smaller than the X-ray generating volume under the electron beam, compositional analysis using EDS is not reliable. However, the particles are large enough to acquire EBSPs with acceptable quality. An EBSP obtained from one of those particles is shown in Fig. 4 (marked by 'Exp.'). In order to identify the phase, dynamical simulation of Kikuchi diffraction patterns of all possible phases [28] was carried out and the calculated patterns are shown in Fig. 4. The simulated patterns of pure nickel and AlNi_3 have the

highest similarity to the experimentally measured pattern. Generally, it is hard to distinguish between these phases (Ni and AlNi₃) unless a very high quality experimental pattern is available. Nevertheless a comparison of finer details enables us to differentiate between these two phases. A 111 zone axis is marked by red rectangles on 'Exp', nickel and AlNi₃ patterns. The center of the zone in nickel has darker triangular contrast while that in AlNi₃ has uniform contrast. The contrast in the 'Exp' pattern matches that in AlNi₃ phase and hence, the particles are most likely AlNi₃.

On the orientation map shown in Fig. 3c, most of the aluminum grains are color coded close to blue, which indicates that the <111> crystallographic direction of the grains is parallel to the deposition growth direction. No reliable EBSP was obtained from the Al₃Ni and Al₃Ni₂ layers, indicating that the layers have grain sizes below the resolution limit of the technique [29]. ICCI has a higher spatial resolution than EBSD and can be used as a supplementary technique [26]. An ICCI micrograph covering partially aluminum and Al₃Ni layers is shown in Fig. 3d. No microstructure is visible in the Al₃Ni layer apart from very fine particles (less than 100 nm in size), which are marked with white arrows on the micrograph. Although some EBSPs were acquired from these particles, their quality was not sufficient for unambiguous phase identification. It is worth noting that AlNi₃ particles (~300 nm in size) are clearly visible on the triple junctions and grain boundaries of aluminium.

120 min. heat treatment

Figs. 5a and 5b respectively show an EDS elemental map for aluminum and an EBSD pattern quality map [30] obtained from the sample heat treatment for 120 min. The elemental map reveals five different layers. The color coding scheme shows the pure nickel in blue, AlNi₃ in green, AlNi in yellow, Al₃Ni₂ in orange and the top layer in red. In the image quality (IQ) map the nickel and AlNi₃ layers are distinct from the Al₃Ni₂ and top porous layers. Al₃Ni₂ layer has two different grain morphologies. Most of the grains are equiaxed whilst the grains in the upper part are elongated and

parallel to the aluminum deposition direction. Fig. 5c is an ICCI of the same location shown in Fig. 5b and clearly reveals that these two different morphologies are separated by a running crack. It is noted that TEM analyses also suggests the elongated grains to be Al_3Ni_2 , though its morphology is different from the lower part of the Al_3Ni_2 layer. The average grain size of the Al_3Ni_2 phase is ~ 800 nm. ICCI also reveals high nickel-containing intermetallics adjacent to the nickel substrate (AlNi and AlNi_3), as seen in Fig. 5c and a higher magnification micrograph of those layers is presented in Fig. 5d. The AlNi and Al_3Ni_2 layers have similar microstructures to one another and cannot be differentiated in the IQ map (Fig. 5b). The average grain size of AlNi is ~ 800 nm, which corresponds roughly to the layer thickness (as measured on Fig. 5d). The AlNi_3 layer is composed of irregular-shaped grains with ~ 300 nm in size on average, which is comparable with the layer thickness.

The Al_3Ni_2 and top porous layers are of high importance for the above-mentioned electrocatalyst synthesis process, namely leaching, and was therefore investigated further by STEM. A low-magnification STEM-BF image of the Al_3Ni_2 layer is shown in Fig. 5e. It is evident that most of the Al_3Ni_2 grains do not contain defects or inclusions although several dislocations in a few grains are observed. Several areas were investigated using high-resolution STEM-BF imaging and no phase other than Al_3Ni_2 was found.

A STEM-HAADF image of the top porous layer in the sample after 120 min. heat treatment is shown in Fig. 6a. It reveals that at least two different types of pores are present. Smaller pores (i.e. voids) have sharp planar interfaces, while larger pores (>50 nm) have irregular shapes with a rim of ~ 15 nm showing darker HAADF contrast. STEM-EDS elemental mapping of a pore of about 100 nm in diameter (Fig. 6b) shows that the rim of the pore is rich in Al and O, with a composition of 38 at.% Al and 62 at.% O. A high resolution STEM image of a rim of a pore, ~ 100 nm in size, is shown in Fig. 6c. The lattice spacing of an area with darker contrast located at the bottom-left

corner of the image was found to be 0.29 nm, which corresponds to {101} planes of Al_3Ni_2 . Fig. 6d shows a fast Fourier transform obtained from the area marked with a box in Fig. 6c. It is assigned to be $\gamma\text{-Al}_2\text{O}_3$ [011] [31], which is also supported from the measured composition mentioned above (Fig. 6b).

4. Discussion:

Formation of all aluminum nickel intermetallics are exothermic [32] and in some processes the generated heat is sufficient to increase the temperature for transformation to a liquid phase [33], [34]. Observing the microstructure of the aluminum layer after heat treatment for 10 min., the top part of microstructure remains unchanged. It therefore follows that the layer must have remained in the solid state and did not transfer to the liquid phase. Thus, possible liquid solid interactions are not considered in this discussion.

All the possible phases in the aluminum-nickel binary system (i.e Al, Al_3Ni , Al_3Ni_2 , AlNi, Al_3Ni_5 , AlNi_3 , and Ni) except Al_3Ni_5 , are present at certain time during heat treatment. Since the number of aluminum atoms is significantly less than those of nickel, it would be expected that the equilibrium state to be FCC nickel with aluminum as solid solution. Formation of layers of high nickel containing intermetallics (AlNi and AlNi_3) starts at a time between 30 to 120 min. as can be seen in Fig. 1. By extending the time (experimentally studied 1440 min.) the thickness of the AlNi and AlNi_3 layers increases. It is expected that at extended periods of time or higher temperatures AlNi and AlNi_3 become the dominant phase(s), however, the kinetics of the process is notably slow at the experimentally studied temperature [35]. Indeed, it has been reported in the literature that a long time is required to achieve thick AlNi layers at relatively low temperatures [36].

The homologous temperature of aluminum at 883 K is approximately 0.95 while that of nickel is 0.51. Thus the diffusion direction from aluminum towards nickel should be expected as reported in earlier publications [37-40]. However, the formation of nickel containing precipitates in the

aluminum layer, (see Fig. 3), strongly suggests the preferential diffusion direction is from the nickel substrate or nickel rich phases formed adjacent to the nickel substrate towards the aluminum layer. Though this may seem counterintuitive, it should be noted that the grain size of the aluminum layer is significantly smaller than that of the nickel substrate before heat treatment (the grain size of the aluminum adjacent to substrate is about 250 nm while the nickel grain size is about 20 μm). The diffusion rate along grain boundaries is much higher than that in the lattice, hence, grain boundaries act as high-diffusivity paths or as diffusion short-circuits [41]. Based on Harrison's classification [41, 42] of diffusion kinetics, diffusion mechanisms are divided into three types: A, B and C, as depicted in Fig. 7. Details of the classification is available in the literature [41, 42], however, for the current discussion, it is sufficient to recall that in type A, grain boundary and volume diffusion are comparable. For type C, diffusion is considered to take place only within the grain boundaries. And type B is somewhat between A and C. In type C, the conditions are such that the volume diffusion is much smaller than the grain boundary diffusion. Though the importance of grains boundaries in diffusion is well-established, knowledge about grain boundary diffusion in intermetallics is rather scarce [43].

Formation of AlNi_3 particles on the triple junctions and grain boundaries of aluminum after 3 min. of heat-treatment shows that grain boundary diffusion is the dominant mechanism of diffusion in the first 3 min. and is of type C. Comparing the samples heat treated for 3 and 10 min. in Fig. 1, shows that the AlNi_3 particles grow in size up to 10 min. of heat treatment, indicating that local grain boundary diffusion of type C is still active¹. At first glance, significant grain growth of as-

¹ It is noteworthy that the formation of a high nickel containing intermetallic (AlNi_3) on the grain boundaries of aluminum is rather peculiar since a high aluminum containing intermetallic such as Al_3Ni is a more intuitive candidate for formation within the aluminum layer. The authors suspected an error and carried out new experiments but similar results were obtained.

deposited at the homologous temperature of 0.95 is expected. However, after heat-treatment for 10 min., the aluminum layer grain size is comparable with that in the as-deposited state (c.f. Fig. 1 and 3a). This observation suggests that the decoration of the boundaries with a nickel/nickel-rich phase that resulted from the fast nickel diffusion reduces the grain boundary mobility significantly. Thus, aluminum grain boundaries are effectively stationary, despite the high homologous temperature. It is worth recalling that diffusion through migrating boundaries is significantly (orders of magnitude) faster than that through stationary grain boundaries [44].

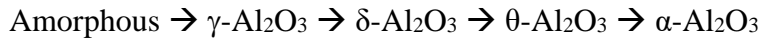
The grain size of aluminum adjacent to the nickel substrate in the as-deposited state is about 250 nm. Unlike the diffusion through the larger grains further away from the substrate, the diffusion of nickel into aluminum through the boundaries of these very fine grains is expected to be of type A in Harrison's classification [41, 42] even though this is not experimentally studied in this work. Nevertheless, the phase transformation of aluminum to the highest aluminum containing intermetallic, i.e. Al_3Ni , takes place. The grain size of this phase is not directly measured in this work but it is either amorphous or crystalline with a size below the resolution limit of both EBSD and ICCI (~50nm) [45]. Amorphous/nanocrystalline phases are metastable and form due to kinetic constraints which suppress formation of the crystalline phase [46]. An enhanced diffusion rate (short-circuit diffusion [41]) is expected in the amorphous / very fine crystalline Al_3Ni . Observing the interface between the Al_3Ni layer and the aluminum grains of about 1 μm in size after 10 min. of heat treatment (Fig. 3a), there is an outward curvature. If the nickel was diffusing faster than aluminum, an inward curvature would form similar to shape shown in Fig. 7. This strongly suggests that the diffusion rate of aluminum is higher than nickel in the Al_3Ni layer. The deposited aluminum layer is consumed within 20 to 30 min. and similarly, the Al_3Ni layer is transformed to Al_3Ni_2 between 30 and 120 min. Other than aluminum reacting with nickel and transforming to Al_3Ni , the AlNi_3 particles sitting on the aluminum grain boundaries are also transformed into Al_3Ni . It seems

that the fine particles in the Al_3Ni layer marked by white arrows in Fig. 3d are a remnant of the high nickel containing particles (AlNi_3) which were not fully transformed. However, as the Al_3Ni_2 front reaches these particles, the very fine particles fully transform. Hence, even after careful examination of the Al_3Ni_2 layer using TEM no particles were detected within the Al_3Ni_2 layer (after 120 min. of heat treatment).

As explained in the introduction, durable electrocatalysts are produced by leaching the aluminum from the Al_3Ni_2 [22, 23], thus, characterization of this phase is of high importance [14]. The very high diffusion coefficient in the Al_3Ni_2 phase [47], enhances the formation of the phase and results in Al_3Ni_2 as the thickest layer [48] in the experimentally studied time (see Fig. 2). This is in agreement with previous investigations, which have reported that Al_3Ni_2 as the fastest growing layer [47, 49-52]. In this study, the Al_3Ni_2 layer is composed of two sublayers with different grain morphologies separated by a crack line (see Fig. 5c). Formation of sub-layers is also reported in AlNi layers [53] and AlNi_3 [35]. That is a clear indication of the Kirkendall effect [53] where the separation boundary of two different morphologies coincides with the Kirkendall plane [54]. When the Kirkendall plane is located inside the layer of a stoichiometric intermetallic phase, the ratio of the intrinsic diffusivities of the elements forming the intermetallic can be estimated by a graphical method [54, 55]. Since the position of the Kirkendall plane is notably distant from the AlNi layer it follows that the intrinsic diffusivity of Al in Al_3Ni_2 is significantly larger than the intrinsic diffusivity of Ni in Al_3Ni_2 . This clearly shows that aluminum is the key diffusing element leading to the formation of Al_3Ni_2 .

The diffusion of oxygen from the furnace atmosphere into the solid phase and formation of oxide(s) has been observed (see Fig. 6). The Al_3Ni_2 phase adjacent to the top surface is porous, and $\gamma\text{-Al}_2\text{O}_3$ is formed in the rims of voids and no alloy oxides are seen. Thus, only aluminum oxides are

considered. The transformation sequence for oxidation of aluminum has been proposed to be as follows [56].



Where the metastable oxides γ , δ and θ are formed at lower temperatures and the transformation to the stable $\alpha\text{-Al}_2\text{O}_3$ takes place at higher temperatures. Thus, the observation of formation of low temperature γ phase is in full agreement with the literature. It is of interest to note that the porous layer forms after the full consumption of the Al_3Ni layer and results from the oxidation of the Al_3Ni_2 layer.

Summary:

The main observations and findings are as follows: (i) grain boundary diffusion of nickel into an aluminum layer brings about the formation of AlNi_3 on the grain boundaries and triple junctions. (ii) Al_3Ni and Al_3Ni_2 are either amorphous or of a grain size below 50nm after 10min. of heat treatment at 883 K. (iii) the curvature of the interface between aluminum grains of 1 μm in size and the Al_3Ni layer after 10 min. of heat treatment indicates that the aluminum is diffusing faster than nickel in Al_3Ni (iv) After 30 min. of heat treatment at 883 K, the aluminum layer is fully transformed, and the dominant phase is Al_3Ni_2 . (v) In the Al_3Ni_2 layer, formation of two different grain morphologies and a running crack line indicate the Kirkendall effect and the separation boundary coincides with the Kirkendall plane. The position of the Kirkendall plane suggests faster diffusion of aluminum in Al_3Ni_2 than that of nickel (v) After Al_3Ni is fully transformed to Al_3Ni_2 a porous structure starts to form on the surface which consists of Al_3Ni_2 and $\gamma\text{-Al}_2\text{O}_3$.

Acknowledgement:

The authors would like to thank Lars Pleth Nielsen and Kristian Rechendorff at The Danish Technological Institute for assisting with the PVD coatings. Ewa Adamsen, Lars Pedersen, John C. Troelsen and Steffen S. Munch at DTU are all acknowledged for their invaluable help. Financial

support from The Energy Technology Development and Demonstration Program in Denmark (EUDP) (project number: 63011-0200) is gratefully acknowledged. The A.P. Møller and Chastine Mc-Kinney Møller Foundation is gratefully acknowledged for the contribution toward the establishment of the Center for Electron Nanoscopy in the Technical University of Denmark.

References:

- [1] H. Choe and D. C. Dunand, "Synthesis, structure, and mechanical properties of Ni–Al and Ni–Cr–Al superalloy foams" *Acta Mater.* 52, (2004) 1283–1295.
- [2] C. E. Campbell, W. J. Boettinger, and U. R. Kattner, "Development of a diffusion mobility database for Ni-base superalloys," *Acta Mater.* 50, (2002) 775–792.
- [3] Q. Wu, S. Li, Y. Ma, and S. Gong, "Study on behavior of NiAl coating with different Ni/Al ratios" *Vacuum* 93, (2013) 37–44.
- [4] G. W. Goward and D. H. Boone, "Mechanisms of formation of diffusion aluminide coatings on nickel-base superalloys" *Oxid. Met.* 3, (1971) 475–495.
- [5] E. G. Colgan, M. Nastasi, and J. W. Mayer, "Initial phase formation and dissociation in the thin-film Ni/Al system" *J. Appl. Phys.* 58, (1985) 4125–4129.
- [6] X.-A. Zhao, E. Ma, and M.-A. Nicolet, "Growth kinetics of NiAl₃ formation on large-grained <Al> substrates" *Mater. Lett.* 5, (1987) 200–202.
- [7] E. Ma, M.-A. Nicolet, and M. Nathan, "NiAl₃ formation in Al/Ni thin-film bilayers with and without contamination" *J. Appl. Phys.* 65, (1989) 2703–2710.
- [8] E. G. Colgan, "A review of thin-film aluminide formation" *Mater. Sci. Rep.* 5, (1990) 1–44.
- [9] J. Noro, A. S. Ramos, and M. T. Vieira, "Intermetallic phase formation in nanometric Ni/Al multilayer thin films" *Intermetallics* 16, (2008) 1061–1065.
- [10] Z. Zhang, B. Gleeson, K. Jung, L. Li, and J. C. Yang, "A diffusion analysis of transient subsurface γ' -Ni₃Al formation during β -NiAl oxidation" *Acta Mater.* 60, (2012) 5273–5283.
- [11] C. Michaelsen, G. Lucadamo and K. Barmak "The early stages of solid-state reactions in Ni/Al multilayer films" *J. Appl. Phys.* 80, (1996) 6689–6698.
- [12] A. S. Edelstein, R. K. Everett, G. Y. Richardson, S. B. Qadri, and E. I. Altman "Intermetallic phase formation during annealing of Al/Ni multilayers" *J. Appl. Phys.* 76, (1994) 7850–7859.
- [13] R. Pretorius, A. M. Vredenberg and F. W. Saris "Prediction of phase formation sequence and phase stability in binary metal-aluminum thin-film systems using the effective heat of formation rule" *J. Appl. Phys.* 70, (1991) 3636–3646.
- [14] R. Wang, H. Chen, Z. Lu, S. Qiu, and T. Ko, "Structural transitions during aluminum leaching of NiAl₃ phase in a Raney Ni–Al alloy" *J. Mater. Sci.* 43, (2008) 5712–5719.
- [15] H. Wendt, H. Hofmann, and V. Plzak, "Materials research and development of electrocatalysts for alkaline water electrolysis" *Mater. Chem. Phys.* 22, (1989) 27–49.
- [16] G. Sheela, M. Pushpavanam, and S. Pushpavanam, "Zinc–nickel alloy electrodeposits for water electrolysis" *Int. J. Hydrog. Energy* 27, (2002) 627–633.
- [17] L. Birry and A. Lasia, "Studies of the hydrogen evolution reaction on Raney nickel-molybdenum electrodes" *Journal of Applied Electrochemistry* 34, (2004) 735–749.
- [18] R. K. Shervedani and A. Lasia, "Kinetics of Hydrogen Evolution Reaction on Nickel-Zinc-Phosphorous Electrodes" *J. Electrochem. Soc.* 144, (1997) 2652–2657.
- [19] P. Los, A. Rami, and A. Lasia, "Hydrogen evolution reaction on Ni-Al electrodes" *J. Appl. Electrochem.* 23 (1993) 135-140.
- [20] G. Schiller, R. Henne, and V. Borck, "Vacuum plasma spraying of high-performance electrodes for alkaline water electrolysis" *J. Therm. Spray Technol.* 4, (1995) 185–194.
- [21] Y. Choquette, H. Ménard, and L. Brossard, "Hydrogen discharge on a Raney nickel composite-coated electrode" *Int. J. Hydrog. Energy* 14, (1989) 637–642.
- [22] C. K. Kjartansdóttir, L. P. Nielsen, and P. Møller, "Development of durable and efficient electrodes for large-scale alkaline water electrolysis" *Int. J. Hydrog. Energy* 38, (2013) 8221–8231.

- [23] C. Kjartansdóttir, M. Caspersen, S. Egelund, and P. Møller, “Electrochemical investigation of surface area effects on PVD Aluminum-nickel as electrocatalyst for alkaline water electrolysis” *Electrochimica Acta* 142, (2014) 324–335.
- [24] H. Alimadadi and K. Pantleon, “Challenges of sample preparation for cross sectional EBSD analysis of electrodeposited nickel films” *30th Risø Int. Symp. Mater. Sci. Nanostructured Met. Appl.* (2008) 183–189.
- [25] M. Schaffer, B. Schaffer, and Q. Ramasse, “Sample preparation for atomic-resolution STEM at low voltages by FIB” *Ultramicroscopy* 114, (2012) 62–71.
- [26] H. Alimadadi, A. B. Fanta, and K. Pantleon, “The complementary use of electron backscatter diffraction and ion channelling imaging for the characterization of nanotwins” *J. Microsc.* 249, (2013) 111–118.
- [27] A. Winkelmann, “Dynamical Simulation of Electron Backscatter Diffraction Patterns” in *Electron Backscatter Diffraction in Materials Science*, J. A. Schwartz, M. Kumar, L. B. Adams, and P. D. Field, Eds. Boston, MA: Springer US, (2009) 21–33.
- [28] T. B. Massalski, H. Okamoto, P. R. Subramanian, L. Kacprzak, and W. W. Scott, *Binary alloy phase diagrams*, vol. 1. American Society for Metals Metals Park, OH, 1986.
- [29] S. Zaeferrer, “On the formation mechanisms, spatial resolution and intensity of backscatter Kikuchi patterns” *Ultramicroscopy*, 107, (2007) 254–266.
- [30] S. I. Wright and M. M. Nowell, “EBSD Image Quality Mapping,” *Microsc. Microanal.* 12 (2005) 72–84.
- [31] G. Gutiérrez, A. Taga, and B. Johansson, “Theoretical structure determination of γ -Al₂O₃,” *Phys. Rev. B*, 65 (2001) 012101.
- [32] D. Shi, B. Wen, R. Melnik, S. Yao, and T. Li, “First-principles studies of Al–Ni intermetallic compounds,” *J. Solid State Chem.*, 182 (2009) 2664–2669.
- [33] K. Morsi, “Review: reaction synthesis processing of Ni–Al intermetallic materials,” *Mater. Sci. Eng. A* 299, (2001) 1–15.
- [34] S. Dong, P. Hou, H. Yang, and G. Zou, “Synthesis of intermetallic NiAl by SHS reaction using coarse-grained nickel and ultrafine-grained aluminum produced by wire electrical explosion” *Intermetallics* 10, (2002) 217–223.
- [35] C. Cserháti, A. Paul, A. A. Kodentsov, M. J. H. van Dal, and F. J. J. van Loo, “Intrinsic diffusion in Ni₃Al system,” *Intermetallics* 11, (2003) 291–297.
- [36] L. S. Castleman and L. L. Seigle, “Formation of intermetallic layers in diffusion couples,” *J Metals* 9, (1957) 1173–1174.
- [37] M. M. P. Janssen and G. D. Rieck, “Reaction diffusion and Kirkendall-effect in the nickel-aluminum system” *Transactions of the Metallurgical Society of AIME* 239, (1967) 1372-1385.
- [38] M. Konieczny, R. Mola, P. Thomas, and M. Kocial, “Processing, microstructure and properties of laminated Ni-intermetallic composites synthesised using Ni sheets and Al foils” *Arch. Metall. Mater.* (2011) 693–702.
- [39] C.-L. Tsao and S.-W. Chen, “Interfacial reactions in the liquid diffusion couples of Mg/Ni, Al/Ni and Al/(Ni)-Al₂O₃ systems” *J. Mater. Sci.* 30, (1995) 5215–5222.
- [40] Q. W. Wang, G. H. Fan, L. Geng, J. Zhang, Y. Z. Zhang, and X. P. Cui, “Formation of intermetallic compound layer in multi-laminated Ni–(TiB₂/Al) composite sheets during annealing treatment” *Micron* 45 (2013) 150–154.
- [41] H. Mehrer, “Diffusion in Solids: Fundamentals, Methods, Materials, Diffusion-Controlled Process,” *Springer Ser. Solid State Sci.* 155, 2007.
- [42] L. G. Harrison, “Influence of dislocations on diffusion kinetics in solids with particular reference to the alkali halides,” *Trans. Faraday Soc.* 57, (1961) 1191–1199.

- [43] H. Mehrer, "Self-Diffusion, Solute-Diffusion and Interdiffusion in Binary Intermetallics," in *Diffusion Foundations*, 2014, vol. 2, pp. 1–72.
- [44] K. Smidoda, C. Gottschalk, and H. Gleiter, "Grain boundary diffusion in migrating boundaries," *Met. Sci.* 13, (1979) 146–148.
- [45] Morgan, John, John Notte, Raymond Hill, and Bill Ward. "An introduction to the helium ion microscope" *Microscopy today* 14, (2006) 24-31.
- [46] U. Gösele and K. N. Tu, "Critical thickness of amorphous phase formation in binary diffusion couples" *J. Appl. Phys.* 66, (1989) 2619–2626.
- [47] T. Philippe, D. Erdeniz, D. C. Dunand, and P. W. Voorhees, "A phase-field study of the aluminizing of nickel" *Philos. Mag.* (2015) 935–947.
- [48] S. R. Shatynski, J. P. Hirth, and R. A. Rapp, "A theory of multiphase binary diffusion" *Acta Metall.* 24, (1976) 1071–1078.
- [49] X. Ren, G. Chen, W. Zhou, C. Wu, and J. Zhang, "Formation and growth kinetics of intermediate phases in Ni-Al diffusion couples" *J. Wuhan Univ. Technol.-Mater Sci Ed*, 24, (2009) 787-790.
- [50] C. Michaelsen and K. Barmak, "Calorimetric determination of NiAl₃-growth kinetics in sputter-deposited Ni/Al diffusion couples" *J. Alloys Compd.* 257, (1997) 211–214.
- [51] Z. D. Xiang, D. Zeng, C. Y. Zhu, D. J. Wu, and P. K. Datta, "Degradation kinetics at 650° C and lifetime prediction of Ni₂Al₃/Ni hybrid coating for protection against high temperature oxidation of creep resistant ferritic steels," *Corros. Sci.* 53, (2011) 3426–3434.
- [52] H. Mehrer, "Diffusion in intermetallics," *Mater. Trans. JIM*, 37, (1996) 1259–1280.
- [53] A. Paul, A. A. Kodentsov, and F. J. J. Van Loo, "Bifurcation of the Kirkendall plane during interdiffusion in the intermetallic compound β -NiAl," *Acta Mater.* 52, (2004) 4041–4048.
- [54] A. Paul, M. J. H. Van Dal, A. A. Kodentsov, and F. J. J. Van Loo, "The Kirkendall effect in multiphase diffusion," *Acta Mater.* 52, (2004) 623–630.
- [55] M. J. H. van Dal, D. G. G. M. Huibers, A. A. Kodentsov, and F. J. J. van Loo, "Formation of Co–Si intermetallics in bulk diffusion couples. Part I. Growth kinetics and mobilities of species in the silicide phases," *Intermetallics* 9, (2001) 409–421.
- [56] M. Sakiyama, P. Tomaszewicz, and G. R. Wallwork, "Oxidation of iron-nickel aluminum alloys in oxygen at 600–800°C" *Oxid. Met.* 13, (1979) 311–330.